



Numerical analysis of small recessed silicon carbide grinding wheels

M.J. Jackson*

Center for Advanced Manufacturing, College of Technology,
Purdue University, West Lafayette, Indiana, USA

* Corresponding author: E-mail address: jacksonmj@purdue.edu

Received 22.09.2010; published in revised form 01.11.2010

Analysis and modelling

ABSTRACT

Purpose: Silicon carbide grinding wheels are tools used in manufacturing industry to form precision components and continue to be used to increase production rates due to their ability to remove high volumes of material at high speeds. There is a demand to increase the speed of rotation of the grinding wheel in order to achieve high removal rates. The increase in speed creates a situation where the grinding machine and the operator are subjected to a possible catastrophic failure of the wheel due to the stresses generated in the coarse brittle structure of the vitrified grinding wheel. The study focused on building and analyzing computer models of grinding wheels with recessed features spinning at different rotational speeds. By employing a computational approach, it was possible to determine the maximum principal stresses in the wheel together with the location of the stresses. The geometry of vitrified wheels considered included a plain-sided rotating wheel and a recessed rotating wheel.

Design/methodology/approach: The paper shows how stresses and factors of safety are calculated in order to predict the bursting speeds of small recessed SiC grinding wheels. The main methods used include finite element analysis and mechanical testing of abrasive materials. The approach of the paper is to integrate the use of numerical analysis techniques and experimental techniques to predict the safe operating conditions of SiC abrasive products.

Findings: Calculations were conducted to determine maximum stress in parallel-sided and recessed cup wheels. Relevant factors of safety and bursting speed were also calculated and compared with experimental data. The paper proves the usefulness and applicability of a method developed for taking account of stress concentrations at the recess of small cup-shaped silicon carbide grinding wheels.

Research limitations/implications: The paper is limited to analyzing small recessed SiC grinding wheels. Further work should focus on large recessed wheels and wheels made with different abrasive grains and bonding materials. The type of porosity distribution should also be investigated.

Practical implications: The paper shows how numerical methods are used to design safe operating conditions for brittle grinding wheels. The methods used show that numerical techniques are suitable for calculating the measures of safety that are an important consideration when designing high speed rotating grinding wheels that can be devastating if allowed to fail in service.

Originality/value: The originality in the paper is revealed owing to the fact that fracture mechanics principles are applied to the prediction of failure of rotating grinding wheels. The paper is of practical importance to mechanical designers who are responsible for the safe design of grinding wheels.

Keywords: Numerical analysis; Finite element methods; Grinding wheels; Silicon carbide; Fracture

Reference to this paper should be given in the following way:

M.J. Jackson, Numerical analysis of small recessed silicon carbide grinding wheels, Journal of Achievements in Materials and Manufacturing Engineering 43/1 (2010) 27-37.

1. Introduction

Grinding wheels that are subjected to high rotational stresses can eventually 'burst' by breaking into smaller fragments that are dominated by bending moments at the onset of fracture. This causes damage to the grinding machine and to the operator if guards inadequately prevent the fragments from penetrating the case of the machine tool. It is of prime importance to be able to calculate the bursting speed of the grinding wheel accurately in order to prevent this from occurring. The energy contained within a fragment of grinding wheel spinning at a certain speed was calculated by Jackson et al. [1]. Methods used to calculate bursting speed that are based on the bending strength of the vitrified material are not accurate and deviate from the true bursting speeds of rotating grinding wheels. Deviations of up to 20% have been observed by Muennich [2]. Table 1 shows the deviations for a variety of grinding wheels with constant bonding formulation, but different abrasive mesh sizes. The grinding wheel was a parallel-sided vitrified wheel with an outer diameter, D , of 610mm, inner diameter, H , of 304.8mm, and a thickness, T , of 20mm.

Table 1.
Calculated and measured bursting speeds of a parallel-sided vitrified grinding wheel

| Abrasive Mesh Size | Calculated Bursting Speed, m/s, (Muennich [2]) | Measured Bursting Speed (m/s) |
|--------------------|------------------------------------------------|-------------------------------|
| 36 | 140.7 | 119.6 |
| 54 | 156.5 | 133 |
| 70 | 166.9 | 142.8 |
| 100 | 183.8 | 153.9 |
| 150 | 196.9 | 164.6 |

Thies [3] and Pompe et al. [4] considered the use of fracture mechanics coupled with the stochastic nature of vitrified compositions to improve the calculation of bursting speed, but unfortunately did not provide any improvement in accuracy.

More uniform deviation of the calculated bursting speed compared to observed bursting speeds. In a recent paper by Behrens and Kammler [6], a procedure is described where bursting speed is calculated using linear elastic fracture mechanics coupled with the determination of rotational stresses using finite element calculations. In their approach, the critical pore size that triggers failure is calculated for a 36-mesh and an 80-mesh vitrified grinding wheel. The stress intensity at the flaw tip is calculated using the mode I stress intensity factor, and is used to calculate the fracture toughness of the abrasive body. The experimental fracture toughness is measured using a single edge v-notch beam loaded in the four-point bending mode to failure. The results are then used in concert with a set of modifying functions that are incorporated into Muennich's equation for calculating bursting speed. The modified equation is:

$$v_{bursting} = \sqrt{\frac{4\sigma_{fracture}}{3 + \nu + (1 - \nu) \cdot \frac{H^2}{D^2} \cdot \rho \cdot f_{\sigma}}} \quad (1)$$

Where $v_{bursting}$ is the bursting speed, $\sigma_{fracture}$ is the fracture strength of the grinding wheel, ν is Poisson's ratio, H is diameter of the bore of the grinding wheel, D is the outer diameter of the grinding wheel, ρ is the density of the vitrified material, and f_{σ} is the stress intensity function at the maximum tangential stress at the outer edge of the bore as a function of the normalized diameter and the depth of the recess. The function f_{σ} is calculated using the following equation:

$$f_{\sigma} = -3.00102x^3 + 4.49064x^2 - 2.58489x + 0.640967y^2 - 2.05676y + 4.98248x^3y^3 - 8.56909x^2y^2 + 6.31512xy + 1.59627 \quad (2)$$

Where $x=P/D$, $y=F/T$, P is the diameter of the recess, T is the thickness of the grinding wheel, F is the depth of the recess, x is the normalized recess diameter, and y is the normalized recess depth. Equations 1 and 2 are valid for the range of F/T between 0.13 and 0.88, and for the range of P/D between 0.36 and 0.96. Equations 1 and 2 are used in the present work for calculating bursting speeds for a variety of different recessed grinding wheels and are compared with experimental bursting speed data.

2. Computational analysis

Dynamic loads on a rotating grinding wheel is defined in the rotating co-ordinate system and while the stiffness and damping terms are the same as those measured in the stationary system, the terms due to inertial resistance are dependent upon the rotation of the grinding wheel. Owing to the porous nature of the grinding wheel body, the dynamic imbalance is magnified in certain parts of the grinding wheel when rotating at certain speeds. The inertial dependent terms need to be determined for a particular wheel structure and are then added to the total impedance of the structure before static and dynamic analyses in the rotating wheel can be performed.

The approach in this study assumes that the co-ordinate system used will rotate at a constant rate about a fixed axis.

accelerating relative to a stationary inertial system and as such, the mass dependent impedance cannot be directly calculated in the rotating system. Therefore, the impedance is calculated for the stationary system then transformed to the rotating system. The development of general transformations is required between stationary and rotating systems. This is accomplished by describing the general vector transformations between stationary and rotating systems, defining the inertial terms in the rotating co-ordinate system, applying these results to develop impedance in the rotating system, and finally, the gyroscopic terms are added to the structural matrices for analyzing the rotating system.

The general transformation of a time-dependent vector from a stationary to a rotating co-ordinate is given by the following:

$$\{v(t)_r\} = [A(t)]\{v(t)_s\} \quad (3)$$

Where $\{v(t)_r\}$ is the rotating co-ordinate system of the time-dependent vector, $[A(t)]$ is the time-dependent transformation matrix from the rotating to the stationary system, and $\{v(t)_s\}$ is the

stationary co-ordinate system of the time-dependent vector. The transformation is valid for any vector, both real and complex. Transformations using complex identities for small angular deviations allow the transformation vector to be described in x-y-z co-ordinates, thus:

$$\begin{cases} x(t)_r \\ y(t)_r \\ z(t)_r \end{cases} = \begin{bmatrix} \cos\theta & \sin\theta & 0 \\ -\sin\theta & \cos\theta & 0 \\ 0 & 0 & 1 \end{bmatrix} \begin{cases} x(t)_s \\ y(t)_s \\ z(t)_s \end{cases} \quad (4)$$

Where,

$\cos\theta = \frac{1}{2}(e^{i\theta} + e^{-i\theta})$ and $\sin\theta = \frac{1}{2}(e^{i\theta} - e^{-i\theta})$, hence,

$$\begin{cases} x(t)_r \\ y(t)_r \\ z(t)_r \end{cases} = \left(\frac{e^{i\theta}}{2} \begin{bmatrix} 1 & -i & 0 \\ i & 1 & 0 \\ 0 & 0 & 0 \end{bmatrix} + \frac{e^{-i\theta}}{2} \begin{bmatrix} 1 & i & 0 \\ -i & 1 & 0 \\ 0 & 0 & 0 \end{bmatrix} + \begin{bmatrix} 0 & 0 & 0 \\ 0 & 0 & 0 \\ 0 & 0 & 1 \end{bmatrix} \right) \begin{cases} x(t)_s \\ y(t)_s \\ z(t)_s \end{cases} \quad (5)$$

Or,

$$\begin{cases} x(t)_r \\ y(t)_r \\ z(t)_r \end{cases} = \left(\frac{e^{i\theta}}{2} [T_1] + \frac{e^{-i\theta}}{2} [T_1]^* + [T_o] \right) \begin{cases} x(t)_s \\ y(t)_s \\ z(t)_s \end{cases} \quad (6)$$

$$[T_1] = \frac{1}{2} \begin{bmatrix} 1 & -i & 0 \\ i & 1 & 0 \\ 0 & 0 & 0 \end{bmatrix} \quad (7)$$

And the conjugate matrix is:

$$[T_1]^* = \frac{1}{2} \begin{bmatrix} 1 & i & 0 \\ -i & 1 & 0 \\ 0 & 0 & 0 \end{bmatrix} \quad (8)$$

$$[T_o] = \begin{bmatrix} 0 & 0 & 0 \\ 0 & 0 & 0 \\ 0 & 0 & 1 \end{bmatrix} \quad (9)$$

Equation 6 can be re-formulated as a transformation from rotating to non-rotating co-ordinates where the progressive and regressive vectors can be written in terms of a non-rotating system, thus,

$$\begin{cases} x(t)_s \\ y(t)_s \\ z(t)_s \end{cases} = \left(\frac{e^{i\theta}}{2} [T_1]^* + \frac{e^{-i\theta}}{2} [T_1] + [T_o] \right) \begin{cases} x(t)_r \\ y(t)_r \\ z(t)_r \end{cases} \quad (10)$$

Inertial forces are calculated using Newton's laws of motion, whilst particles contained within the body are defined as position vectors. The inertial force on a particle whose position is measured relative to a rotating co-ordinate system is,

$$\{F(t)_{inertial}\}_r = - \left([M] \left(\frac{d^2\{\rho(t)_r\}}{dt^2} \right) - \Omega [B^c] \left(\frac{d\{\rho(t)_r\}}{dt} \right) - \Omega^2 [K^c] \{\rho(t)_r\} \right) \quad (11)$$

Where,

$$[M] = \begin{bmatrix} m & 0 & 0 \\ 0 & m & 0 \\ 0 & 0 & m \end{bmatrix} \quad (12)$$

$$[B^c] = \begin{bmatrix} 0 & 2m & 0 \\ -2m & 0 & 0 \\ 0 & 0 & 0 \end{bmatrix} \quad (13)$$

$$[K^c] = \begin{bmatrix} m & 0 & 0 \\ 0 & m & 0 \\ 0 & 0 & 0 \end{bmatrix} \quad (14)$$

The structural impedance of the rotating structure requires inertial force terms that are functions of the time varying position of mass of the particle. Therefore, the position vector can be written in terms of an initial component and a time-varying component. The equation of motion for a particle in a rotating elastic disk with no externally applied forces is given by,

$$\Omega^2 [K^c] \{\rho_r\} = \left([M] \left(\frac{d^2\{u(t)_r\}}{dt^2} \right) + ([B] - \Omega [B^c]) \left(\frac{d\{u(t)_r\}}{dt} \right) + ([K] - \Omega^2 [K^c]) \{u(t)_r\} \right) \quad (15)$$

Equation 15 shows that the centripetal loading is always present in the rotating structure. For accurate analysis of the rotating structure, a differential stiffness term is added,

$$[M] \left(\frac{d^2\{\Delta\alpha(t)_r\}}{dt^2} \right) + ([B] - \Omega [B^c]) \left(\frac{d\{\Delta\alpha(t)_r\}}{dt} \right) + ([K] + \Omega^2 [K^d] - \Omega^2 [K^c]) \{\Delta\alpha(t)_r\} = 0 \quad (16)$$

Equation 16 is used to determine the motion of a rotating structure about the deformation due to centripetal loading. For the case of a rotating recessed grinding wheel, finite element computations are modelled as rigid bodies with added gyroscopic effects at critical speeds of rotation. At selected speeds, dynamic out-of-balance forces are predicted using rotation-dependent terms. The finite element programme used in the present work is MSC. NastranTM and the procedure to add rotation dependent terms is done by calculating the terms then adding them to the structural damping and stiffness matrices, and by starting the analysis with the modified matrices.

3. Experimental methods

The experimental part of the current work is focused on demonstrating the magnitude of stresses in recessed vitrified grinding wheels, calculating bursting speeds of the said wheels, and comparing those speeds with experimentally determined bursting speeds. The experimental section also focuses on

measuring selected mechanical properties in order to calculate factors of safety for a variety of small cup grinding wheels.

3.1. Computational stress analysis

A solid model of a parallel-sided grinding wheel was created using the Solid Works™ software package. The dimensions of the wheels and associated solid models are shown in Figure 1. The grinding wheel possessed an outer diameter of 508mm and an inner diameter of 304.8mm. The grinding wheel was composed of a mixture of silicon carbide abrasive grain mixed with a glass-clay bonding agent.

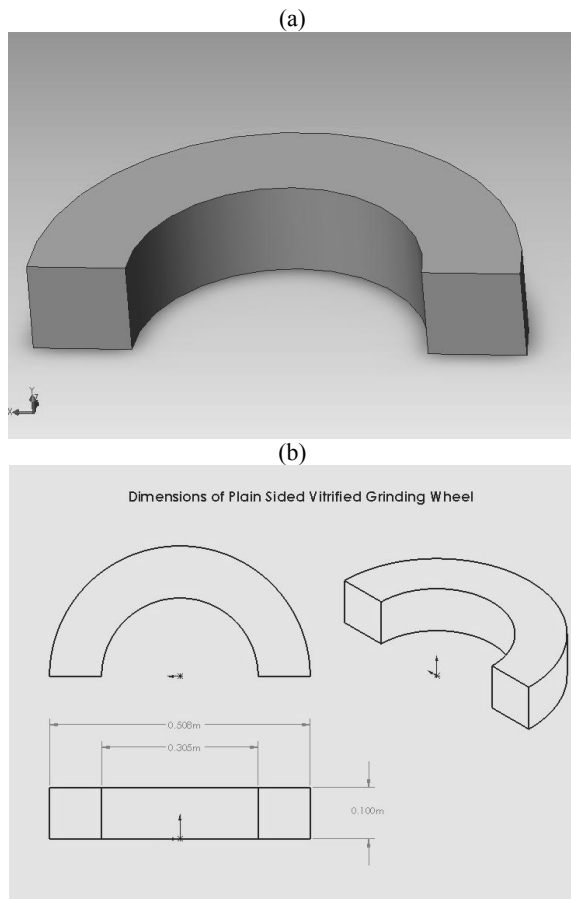


Fig. 1. (a) Solid Works™ model of the parallel-sided grinding wheel, (b) and dimensions associated with the parallel-sided silicon carbide grinding wheel

The grade of the wheel was GC36J8V, indicating a 36-mesh grain size, fairly open 8 structure, J-grade vitrified structure. The model was imported into the MSC. Patran™ software programme in the form of a .xmt file, or Parisolid Model. The model was then meshed and the global edge length to optimize the mesh density of the solid was determined by means of convergence. The convergence model is shown in Figure 2. Material properties (Table 2) were assigned to the solid model of the wheel and

constraints and boundary conditions were applied to the model. The centre of the wheel was constrained in the translational x-, y-, and z-directions as well as in the rotational x- and z-directions. The y-rotational direction was left unconstrained because it is the axis in which the wheel rotates. An inertial velocity was then applied to the entire solid in order to simulate the rotation of the grinding wheel about the y-axis. Visual results, or fringe plots, showing where the maximum principal stress occurred and the quantity of that stress, was the final output of the analysis. The results are shown in the experimental results section of the paper.

Table 2.

Properties of the vitrified grinding wheel structure

| Property | Value |
|----------------------------------------------------|------------------|
| Young's modulus of elasticity (Nm^{-2}) | 55×10^9 |
| Poisson's ratio | 0.22 |
| Density (kg m^{-3}) | 2255 |

Convergence of Mesh for a Plain Sided Fixed Rotating Grinding Wheel

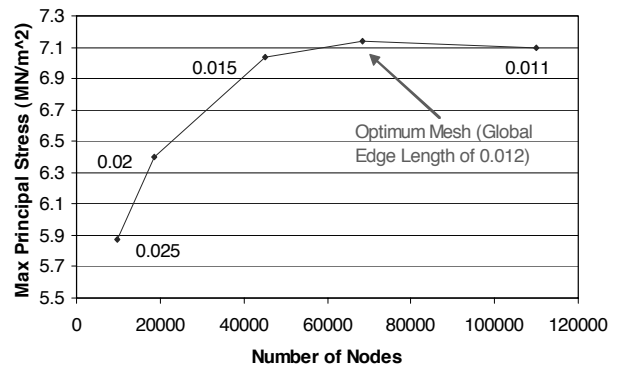


Fig. 2. Convergence of the solid model mesh showing an optimized global edge length of 0.012mm

Figure 3 shows the dimensions and the solid model of a recessed, small cup vitrified grinding wheel. The grinding wheel possessed an outer diameter of 250mm and an inner diameter of 76mm. The grinding wheel was composed of a mixture of silicon carbide abrasive grain mixed with a glass-clay bonding agent. The grade of the wheel was GC36J8V, indicating a 36-mesh grain size, fairly open 8 structure, J-grade vitrified structure. The recessed model was also imported into the MSC. Patran™ software programme in the form of a .xmt file, or Parisolid Model. Again, material properties (Table 1) were assigned to the solid model of the wheel and constraints and boundary conditions were applied to the model. The centre of the wheel was constrained in the translational x-, y-, and z-directions as well as in the rotational x- and z-directions. The y-rotational direction was left unconstrained because it is the axis in which the wheel rotates. An inertial velocity was then applied to the entire solid in order to simulate the rotation of the grinding wheel about the y-axis. Visual results, or fringe plots, showing where the maximum principal stress occurred and the quantity of that stress, was the final output of the analysis.

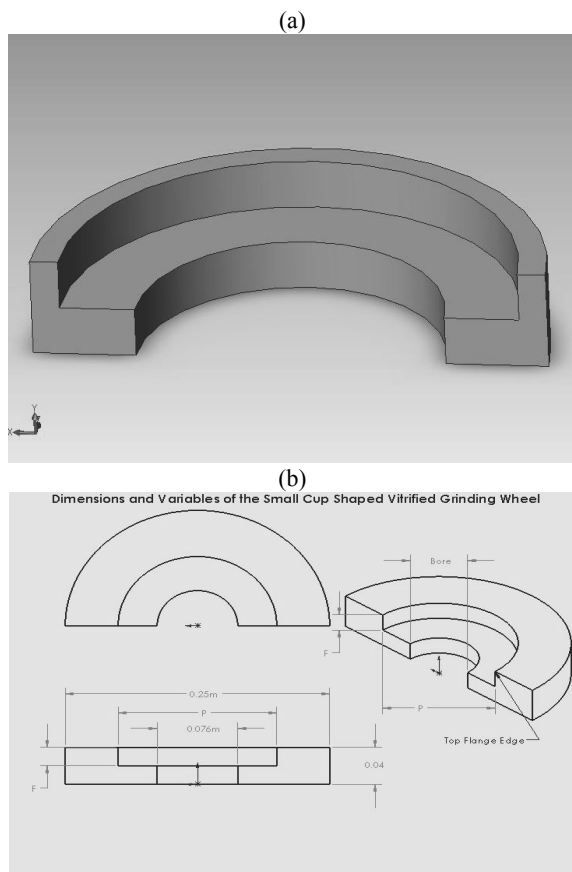


Fig. 3. (a) Solid Works™ model of the recessed, small cup grinding wheel, (b) and dimensions associated with the recessed, small cup silicon carbide grinding wheel

3.2. Determination of bursting speed

In order to measure the bursting speed of a grinding wheel, it is necessary to rotate the wheel at its maximum speed when failure occurs. In order to achieve this in a safe way, the grinding wheel is located in rotating frame that it buried in the ground surrounded by reinforced concrete baffles that absorbs the energy of impacting parts of the broken grinding wheel. The containment structure was lined with an energy absorbing foam, of which the top could be opened for access. The enclosure contained a roll grinding wheel head with the workpiece drive and in-feed mechanism removed. The wheel head was modified and fitted with a spindle cartridge designed for speeds up to 3000 rpm. Once the grinding wheels were mounted and bolted on the spindle housing, the speed of the wheel was increased until the wheel fractured about the spindle, usually into three to four parts. The grinding wheel was inspected for failure and the failure speed was recorded. The grinding wheel was photographed and points of failure recorded for posterity.

3.3. Determination of mechanical properties of grinding wheels

Two types of grinding wheels were used to determine the mechanical properties of the abrasive structures. The experimental determination of density and Poisson's ratio was demonstrated in a previous paper by the author [1], and involves using a pycnometer and a universal tensile testing machine. The grinding wheel structures were manufactured in the form of tensile test bars and parallel-sided and recessed grinding wheels. The grains of abrasive were mixed with a clay-glass bonding formulation, molded, and pressed to the correct density to provide the correct amount of porosity and structure. The samples were fired in an electric furnace to a temperature of approximately 1060°C. The samples were cooled slowly until their appropriate hardness is reached. Hardness was measured by measuring the torque resistance of an indenting chisel that was rotated at a prescribed force. Once cooled, samples of grinding wheel were polished and mounted in resin moulds. Figure 4 shows the polished microstructure of a vitrified grinding wheel of known specification, GC36J8V, whilst Figure 5 shows a microstructure with a known specification of GC80J8V. From the micrographs the critical pore size is found by measuring the distance between abrasive grains. The critical pore size allows one to calculate the fracture toughness of the abrasive structures. The measured fracture toughness is determined by stressing an abrasive structure to failure using notched test bars in the four-point bending mode I using a universal testing machine.

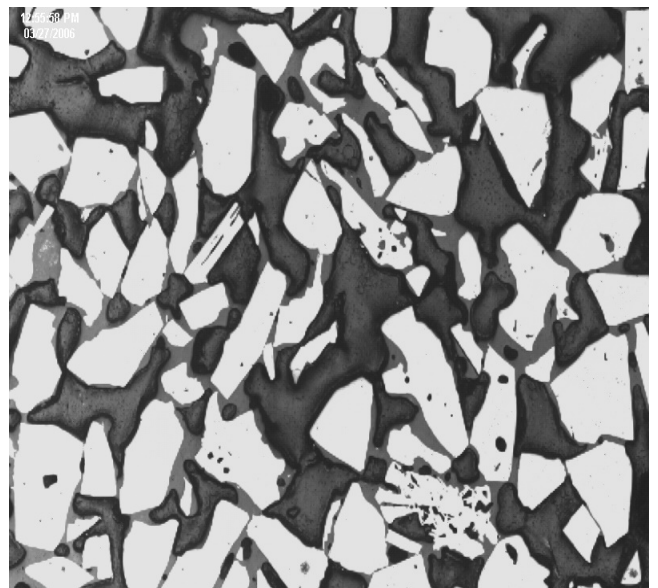


Fig. 4. Polished microstructure of the GC80J8V grinding wheel. Light areas indicate the abrasive grain, grey areas show the vitrified bonding system, and the darker areas show porosity. Bubbles within the pores are features associated with the resin that has infiltrated the open pores. Closed pores are shown with the abrasive grains and the bonding bridges. Average distance between grains is approximately 1.8mm

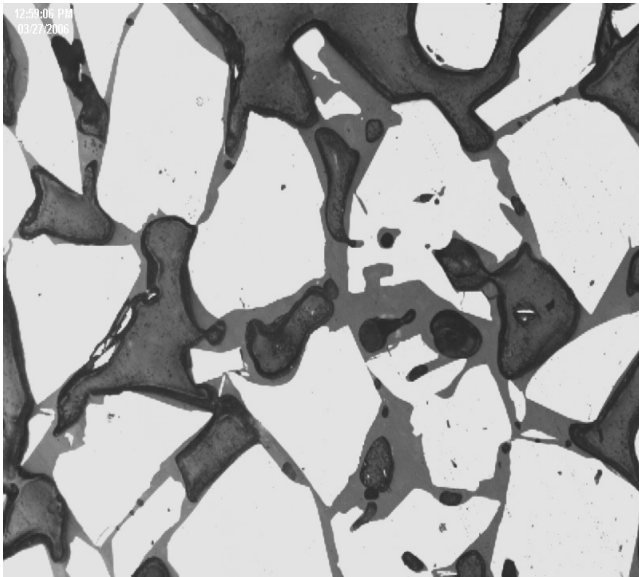


Fig. 5. Polished microstructure of the GC36J8V grinding wheel. Light areas indicate the abrasive grain, grey areas show the vitrified bonding system, and the darker areas show porosity. Bubbles within the pores are features associated with the resin that has infiltrated the open pores. Closed pores are shown with the abrasive grains and the bonding bridges. Average distance between grains is approximately 0.7mm

4. Experimental results

Computational Stress Analysis

The computational stress analysis was performed on both parallel-sided and small cup grinding wheel structures and the results are shown in this section of the paper. Figure 6 shows the computed circumferential stress as a function of distance from the bore to the edge of the wheel spinning at 35 m/s.

4.1. Parallel-sided grinding wheels

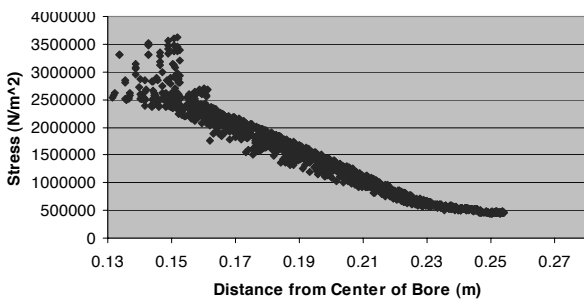


Fig. 6. Calculated circumferential stress distribution as a function of distance from the center of the bore of the grinding wheel spinning at 35 ms⁻¹

The maximum stress at the bore is approximately 3.75 MN/m². Figure 7 shows the finite element mesh and boundary conditions for the parallel sided grinding wheel spinning at 45 m/s. The associated fringe plot showing the magnitude of circumferential stress is shown in Figure 8. The indicated maximum stress is approximately 7.14 MN/m².

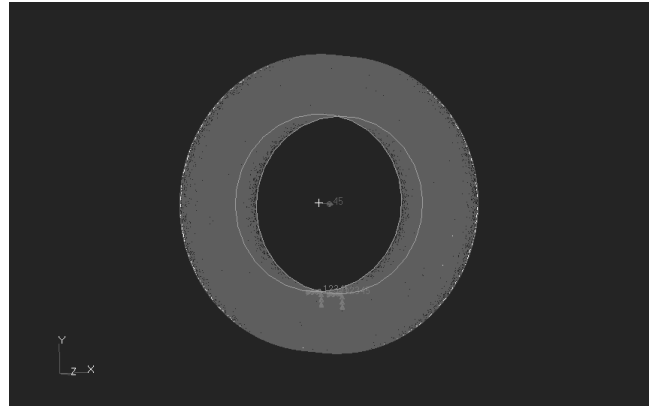


Fig. 7. Mesh and Boundary Conditions of a Plain Sided Grinding Wheel spinning at 45 m/s

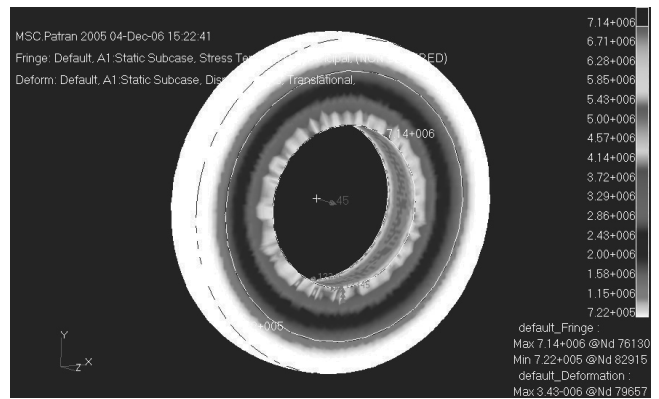


Fig. 8. Fringe Plot of a Plain Sided Grinding Wheel spinning at 45 m/s

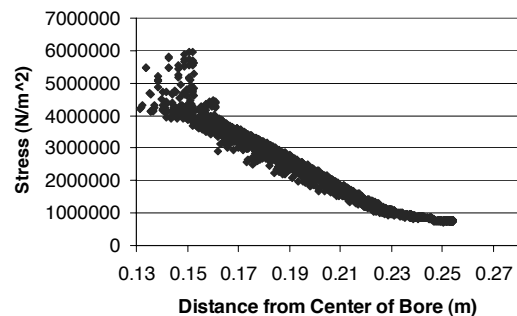


Fig. 9. Calculated circumferential stress distribution as a function of distance from the center of the bore of the grinding wheel spinning at 45 ms⁻¹

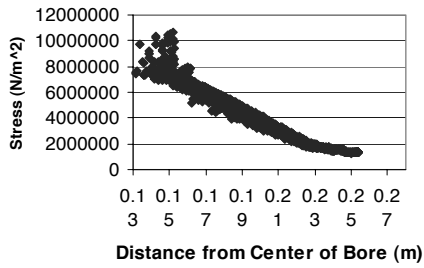


Fig. 10. Calculated circumferential stress distribution as a function of distance from the center of the bore of the grinding wheel spinning at 60 ms^{-1}

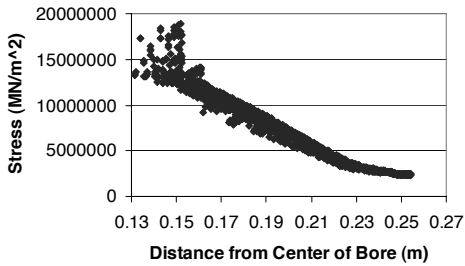


Fig. 11. Calculated circumferential stress distribution as a function of distance from the center of the bore of the grinding wheel spinning at 80 ms^{-1}

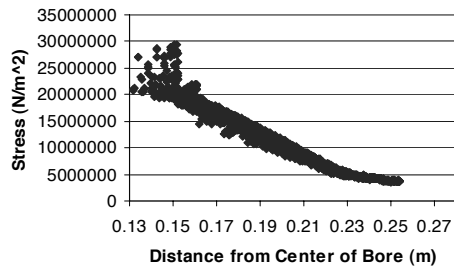


Fig. 12. Calculated circumferential stress distribution as a function of distance from the center of the bore of the grinding wheel spinning at 100 ms^{-1}

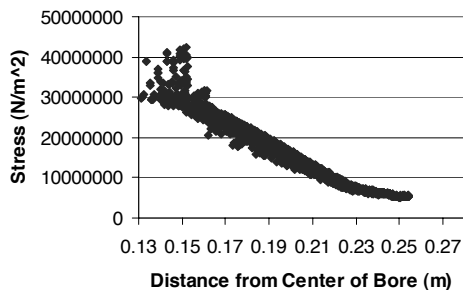


Fig. 13. Calculated circumferential stress distribution as a function of distance from the center of the bore of the grinding wheel spinning at 120 ms^{-1}

Figures 9-13 show the magnitudes of stress throughout a parallel-sided grinding wheel for a wheel rotating at 45, 60, 80, 100, and 120 m/s. The maximum circumferential stress occurs at the bore and the stresses are approximately, 6, 13, 19, 30, and 43 MN/m^2 , respectively.

4.2. Small cup recessed grinding wheels

In contrast to parallel-sided grinding wheels, MSC Patran was used to calculate the maximum principal stress for a variety of small cup recessed grinding wheels. Figure 14 shows a fringe plot for a wheel spinning at 45 m/s ($P=100$ and $F=10$). The maximum stress occurs at the bore and is circumferential in nature. The magnitude of the stress is approximately 3.51 MN/m^2 . Figure 15 shows a fringe plot for a recessed wheel spinning at 45 m/s. The maximum stress occurs at the bore and is approximately 4.38 MN/m^2 . The geometry of the cup wheel is $P=100$ and $F=20$.



Fig. 14. Fringe Plot of Small Cup Shaped Grinding Wheel spinning at 45 m/s ($P=100$ $F=10$)

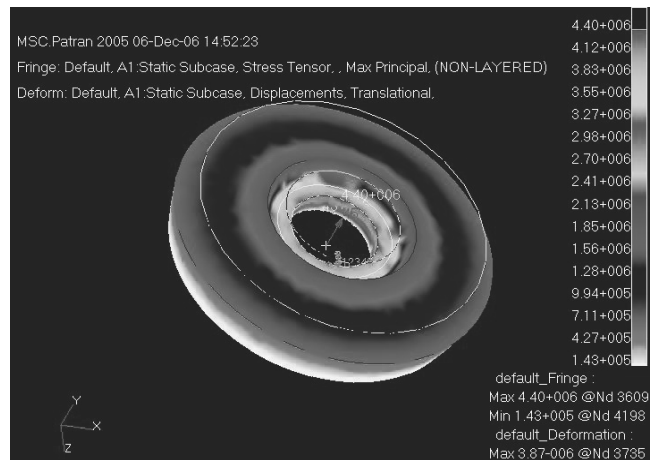


Fig. 15. Fringe Plot of Small Cup Shaped Grinding Wheel spinning at 45 m/s ($P=100$ $F=20$)

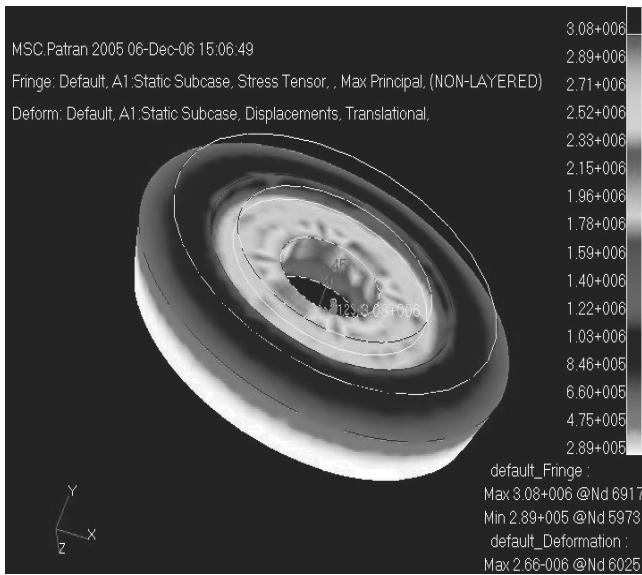


Fig. 16. Fringe Plot of Small Cup Shaped Grinding Wheel spinning at 45 m/s (P=150 F=10)

Figure 16 shows a fringe plot for a recessed wheel spinning at 45 m/s. The maximum stress occurs at the bore and is approximately 3.08 MN/m². The geometry of the cup wheel is P=150 and F=10.

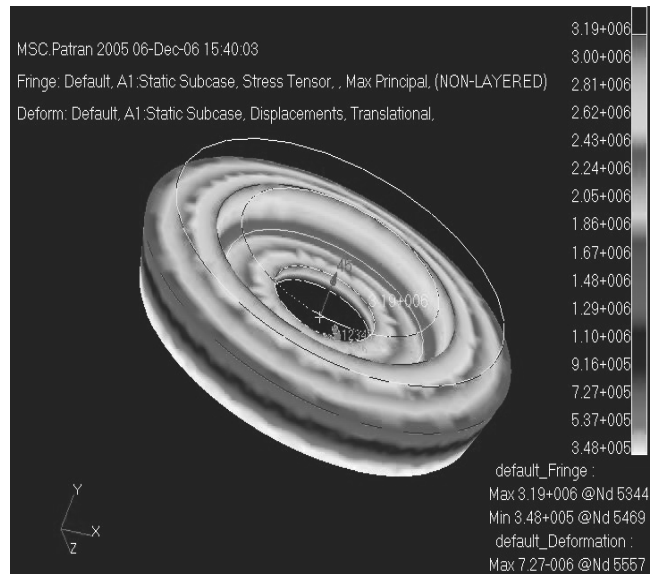


Fig. 18. Fringe Plot of Small Cup Shaped Grinding Wheel spinning at 45 m/s (P=150 F=30)

Figure 18 shows a fringe plot for a recessed wheel spinning at 45 m/s. The maximum stress occurs at the bore and is approximately 3.19 MN/m². The geometry of the cup wheel is P=150 and F=30.

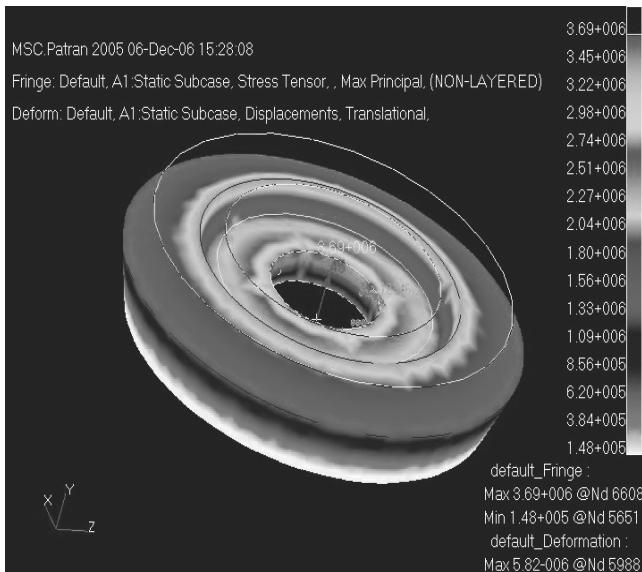


Fig. 17. Fringe Plot of Small Cup Shaped Grinding Wheel spinning at 45 m/s (P=150 F=20)

Figure 17 shows a fringe plot for a recessed wheel spinning at 45 m/s. The maximum stress occurs at the bore and is approximately 3.69 MN/m². The geometry of the cup wheel is P=150 and F=20.

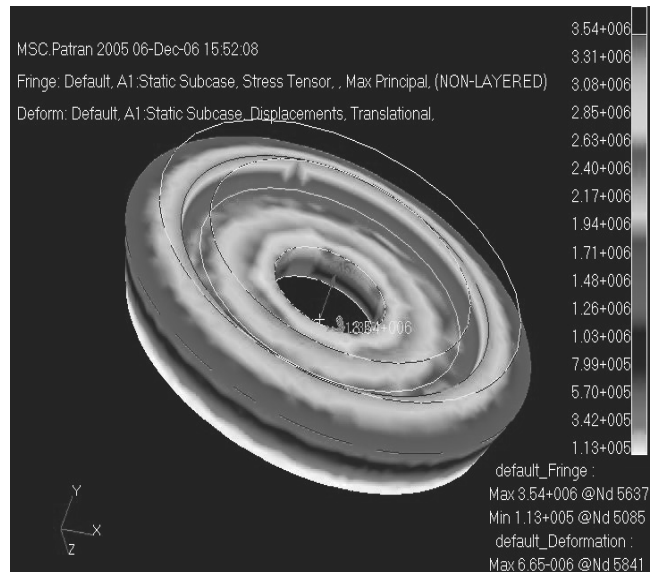


Fig. 19. Fringe Plot of Small Cup Shaped Grinding Wheel spinning at 45 m/s (P=180 F=20)

Figure 19 shows a fringe plot for a recessed wheel spinning at 45 m/s. The maximum stress occurs at the bore and is approximately 3.54 MN/m². The geometry of the cup wheel is P=180 and F=20.

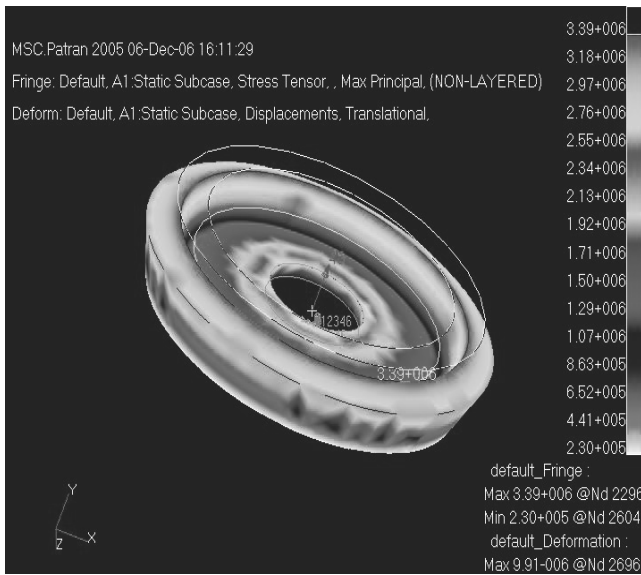


Fig. 20. Fringe Plot of Small Cup Shaped Grinding Wheel spinning at 45 m/s (P=200 F=30)

Figure 20 shows a fringe plot for a recessed wheel spinning at 45 m/s. The maximum stress occurs at the bore and is approximately 3.38 MN/m². The geometry of the cup wheel is P=200 and F=30. Once the rotational stresses were calculated, the small cup grinding wheels were rotated to failure. Figure 21 shows a fractured small cup recessed grinding wheel. The speed at which failure occurred was recorded and compared to the analytical calculation. Factors of safety for each wheel were also recorded and the complete set of data is shown in Table 3. Micrographs of fractured surfaces are shown in Figures 22-24 at various magnifications. The images show that failure occurred by grain fracture and by fracture at the bond bridge interface.



Fig. 21. Exploded View of Cup Shaped Vitrified Grinding Wheel After Recovery From the Burst Chamber

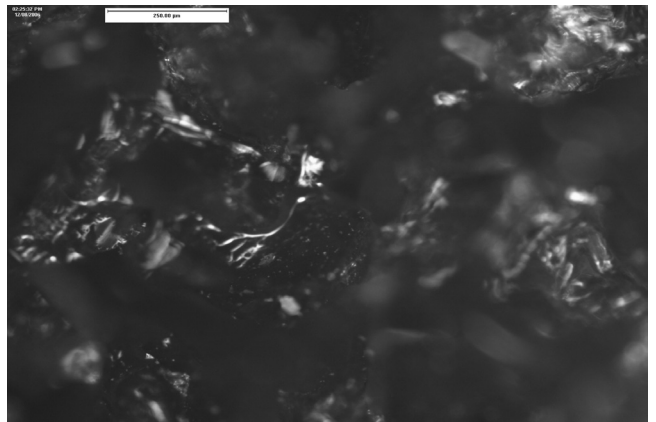


Fig. 22. Micrograph of Vitrified Grinding Wheel Magnified at 5X Magnification

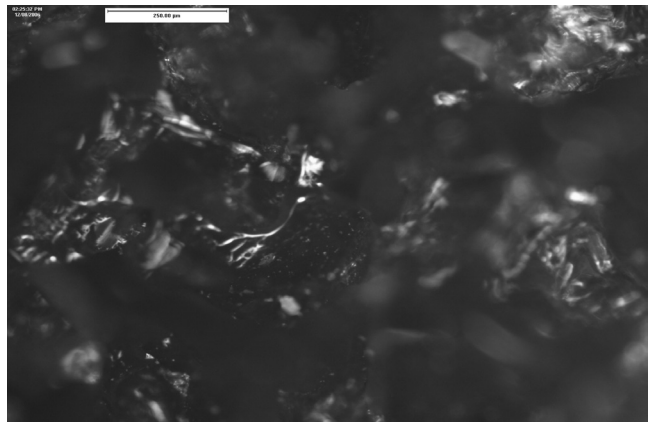


Fig. 23. Micrograph of Cup Shaped Vitrified Grinding Wheel Magnified at 10X Magnification. Failure has occurred by failure at the bond bridge interface. The area that is focus shows the end of a bond bridge that was previously connected to an abrasive grain

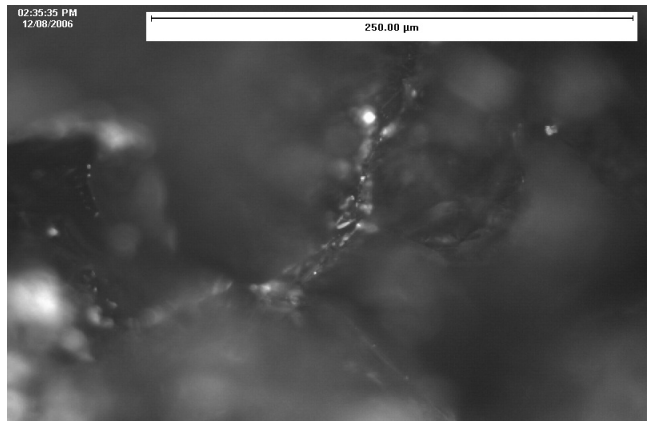


Fig. 24. Micrograph of Cup Shaped Vitrified Grinding Wheel Magnified at 10X Magnification. The micrograph shows a partially fractured abrasive grain

Table 3.

Mechanical Property Data Concerning the Operating Conditions for Various Grinding Wheels with Varying Geometry and Rotational Speeds

Rotational Speed = 45 m/s

| Cup Geometry (mm) | Maximum Circumferential Stress (MN/m ²) | Factor of Safety | x | y | f _g | Calculated Bursting Speed (m/s) | Experimental Bursting Speed (m/s) |
|-------------------|-----------------------------------------------------|------------------|------|------|----------------|---------------------------------|-----------------------------------|
| P=100, F=10 | 3.51 | 16 | 0.4 | 0.25 | 1.16 | 480 | 456 |
| P=100, F=20 | 4.38 | 12.7 | 0.4 | 0.5 | 1.18 | 476 | 461 |
| P=150, F=10 | 3.08 | 18.2 | 0.6 | 0.25 | 1.3 | 452 | 460 |
| P=150, F=20 | 3.69 | 15.2 | 0.6 | 0.5 | 1.4 | 437 | 450 |
| P=150, F=30 | 3.19 | 17.5 | 0.6 | 0.75 | 1.39 | 439 | 452 |
| P=180, F=20 | 3.54 | 15.8 | 0.72 | 0.5 | 1.47 | 427 | 432 |
| P=200, F=30 | 3.38 | 16.5 | 0.8 | 0.75 | 1.46 | 428 | 430 |

Rotational Speed = 60 m/s

| Cup Geometry (mm) | Maximum Circumferential Stress (MN/m ²) | Factor of Safety | x | y | f _g | Calculated Bursting Speed (m/s) | Experimental Bursting Speed (m/s) |
|-------------------|-----------------------------------------------------|------------------|------|------|----------------|---------------------------------|-----------------------------------|
| P=100, F=10 | 6.24 | 9 | 0.4 | 0.25 | 1.16 | 480 | 456 |
| P=100, F=20 | 7.81 | 7.1 | 0.4 | 0.5 | 1.18 | 476 | 461 |
| P=150, F=10 | 5.46 | 10.24 | 0.6 | 0.25 | 1.3 | 452 | 460 |
| P=150, F=20 | 6.55 | 8.54 | 0.6 | 0.5 | 1.4 | 437 | 450 |
| P=150, F=30 | 5.65 | 9.9 | 0.6 | 0.75 | 1.39 | 439 | 452 |
| P=180, F=20 | 6.28 | 8.9 | 0.72 | 0.5 | 1.47 | 427 | 432 |
| P=200, F=30 | 6.02 | 9.3 | 0.8 | 0.75 | 1.46 | 428 | 430 |

Rotational Speed = 90 m/s

| Cup Geometry (mm) | Maximum Circumferential Stress (MN/m ²) | Factor of Safety | x | y | f _g | Calculated Bursting Speed (m/s) | Experimental Bursting Speed (m/s) |
|-------------------|-----------------------------------------------------|------------------|------|------|----------------|---------------------------------|-----------------------------------|
| P=100, F=10 | 14.1 | 4 | 0.4 | 0.25 | 1.16 | 480 | 456 |
| P=100, F=20 | 17.55 | 3.2 | 0.4 | 0.5 | 1.18 | 476 | 461 |
| P=150, F=10 | 12.26 | 4.5 | 0.6 | 0.25 | 1.3 | 452 | 460 |
| P=150, F=20 | 14.8 | 3.8 | 0.6 | 0.5 | 1.4 | 437 | 450 |
| P=150, F=30 | 12.6 | 4.4 | 0.6 | 0.75 | 1.39 | 439 | 452 |
| P=180, F=20 | 14.1 | 4 | 0.72 | 0.5 | 1.47 | 427 | 432 |
| P=200, F=30 | 13.5 | 4.1 | 0.8 | 0.75 | 1.46 | 428 | 430 |

Rotational Speed = 125 m/s

| Cup Geometry (mm) | Maximum Circumferential Stress (MN/m ²) | Factor of Safety | x | y | f _g | Calculated Bursting Speed (m/s) | Experimental Bursting Speed (m/s) |
|-------------------|-----------------------------------------------------|------------------|------|------|----------------|---------------------------------|-----------------------------------|
| P=100, F=10 | 27.1 | 2 | 0.4 | 0.25 | 1.16 | 480 | 456 |
| P=100, F=20 | 34.2 | 1.6 | 0.4 | 0.5 | 1.18 | 476 | 461 |
| P=150, F=10 | 23.6 | 2.4 | 0.6 | 0.25 | 1.3 | 452 | 460 |
| P=150, F=20 | 28.5 | 2 | 0.6 | 0.5 | 1.4 | 437 | 450 |
| P=150, F=30 | 24.55 | 2.3 | 0.6 | 0.75 | 1.39 | 439 | 452 |
| P=180, F=20 | 27.33 | 2 | 0.72 | 0.5 | 1.47 | 427 | 432 |
| P=200, F=30 | 26.2 | 2.15 | 0.8 | 0.75 | 1.46 | 428 | 430 |

5. Discussion

The main objective of the contents of this paper focus on the stresses developed during the safe operation of small cup-shaped grinding wheels accounting for the stress concentration experienced at the recess of such grinding wheels. Principal stresses were computed using a finite element programme where rotation dependent terms were modified by adding structural damping and stiffness matrices. It was discovered that the maximum principal stress occurs at the bore of the small cup-shaped recessed grinding wheels and increases with rotational speed. Table 3 shows the magnitude of those stresses for various geometry and peripheral operating speed. Convergence of the finite element results occurred with a mesh that possesses a global edge length of 0.012mm with approximately 68,000 nodes for the recessed cup shape. The range of stresses increased from 3.51 MN/m² to a maximum of 34.2 MN/m² as a function of rotational speed. The measured tensile strength of the abrasive grain material used was approximately 54 MN/m². This yielded safety factors in the range between 1.6 and 18. The calculated bursting speeds are also shown in Table 3 and are compared with experimentally determined bursting speed. The calculated bursting speeds are within $\pm 5\%$ of the measured bursting speeds and show remarkable accuracy when using the method developed by Behrens and Kammler [6]. Their method takes account of stress concentrations that occur at the recesses of cup-shaped grinding wheels. Polished micrographs of the structure of cup wheels also allowed the author to measure the critical pore size in order to measure the fracture toughness of the cup wheels. The measured fracture toughness for the 80 grain size cup wheel was 2.11 M Pa \sqrt{m} , and 1.84 M Pa \sqrt{m} for a 36 grain size cup wheel. The standard deviation was 10% and 12%, respectively.

6. Conclusions

1. For both parallel-sided wheels and recessed cup wheels, the maximum principal stress acted circumferentially at the bore of the grinding wheel;
2. For the recessed cup-shaped grinding wheels, the factor of safety varied from 1.6 to 18 depending on their rotational speed;
3. The measured fracture toughness for the 80 grain size cup wheel was 2.11 M Pa \sqrt{m} , and 1.84 M Pa \sqrt{m} for a 36 grain size cup wheel. The standard deviation was 10% and 12%, respectively.
4. The method developed by Behrens and Kammler [6] proved to yield accurate values of bursting speed when compared to experimentally determined bursting speeds.

References

- [1] M.J. Jackson, N. Barlow, B. Mills, W.B. Rowe, Mechanical Design Safety of Vitreous Bonded Cylindrical Grinding Wheels, *British Ceramic Transactions* 94/6 (1995) 221-229.
- [2] H. Muennich, Beitrag zur Sicherheit von umlaufenden Schleifkoerpern von keramisch gebundenen Schleifscheiben, Ph. D. Thesis, University of Hannover, 1956.
- [3] J. Thies, Non-destructive and cracking mechanics investigations on ceramic grinding wheels, Ph. D. Thesis University of Hannover, 1986.
- [4] W. Pompe, D. Haupt, H.J. Weiss, Aspects of static cracking strength of ceramic grinding wheels, *Ceramic Forum International* 60/8 (1983) 296-300.
- [5] D. Mewes, O. Mewes, S. Schulz, Grinding wheels strength as a process safety factor, *Maschinenmarkt* 40 (2000) 38-41.
- [6] J.A. Behrens, M. Kemmler, Numerical and Experimental Analysis of the Breaking Behaviour of Vitrified Bonded Grinding Wheels, *Ceramic Forum International* 82/11 (2005) 47-52.